High-Performance Lithium-Sulfur Batteries with a Self-Supported, 3D Li_2S-Doped Graphene Aerogel Cathodes

*Guangmin Zhou, Eunsu Paek, Gyeong S. Hwang, and Arumugam Manthiram**

Lithium-sulfur (Li-S) batteries are being considered as the next-generation high-energy-storage system due to their high theoretical energy density. However, the use of a lithium-metal anode poses serious safety concerns due to lithium dendrite formation, which causes short-circuiting, and possible explosions of the cell. One feasible way to address this issue is to pair a fully lithiated lithium sulfide (Li_2S) cathode with lithium metal-free anodes. However, bulk Li_2S particles face the challenges of having a large activation barrier during the initial charge, low active-material utilization, poor electrical conductivity, and fast capacity fade, preventing their practical utility. Here, the development of a self-supported, high capacity, long-life cathode material is presented for Li-S batteries by coating Li_2S onto doped graphene aerogels via a simple liquid infiltration–evaporation coating method. The resultant cathodes are able to lower the initial charge voltage barrier and attain a high specific capacity, good rate capability, and excellent cycling stability. The improved performance can be attributed to the (i) cross-linked, porous graphene network enabling fast electron/ion transfer, (ii) coated Li_2S on graphene with high utilization and a reduced energy barrier, and (iii) doped heteroatoms with a strong binding affinity toward Li_2S/lithium polysulfides with reduced polysulfide dissolution based on first-principles calculations.

1. Introduction

The increasing requirement for electrical vehicles and large-scale smart grid has promoted the development of advanced energy storage systems that go beyond the currently used Li-ion batteries (LIBs).[1,2] Lithium-sulfur (Li-S) batteries, based on the conversion-reaction chemistry instead of the intercalation-reaction mechanism, are regarded as one of the most promising candidates with a high theoretical energy density of 2600 Wh kg^{-1}.[3–6] Sulfur, a petroleum by-product, is inexpensive and abundant with no or little environmental impact. However, the practical implementation of Li-S batteries has been impeded by the intrinsic electronically insulating properties of sulfur and its discharge products, rapid capacity fading/low Coulombic efficiency originating from polysulfide shuttle effect, and the large volume change occurring between sulfur and lithium sulfide (Li_2S), causing electrode structure damage as a result of different densities.[7–13] Another growing concern for efficient Li-S batteries is the nonuniform deposition of lithium during cycling, leading to lithium dendrite formation, causing short-circuiting within the cell.[14,15]

Replacement of sulfur with Li_2S is a feasible way to avoid the safety issues that arise with employing metallic lithium since Li_2S is compatible with lithium metal-free anodes such as silicon, tin, and carbonaceous materials.[16–18] Other advantages of Li_2S include: (i) a high theoretical specific capacity of 1166 mAh g^{-1}, more than five times higher compared to the traditional intercalation-type cathode materials and (ii) the lack of volume expansion after cell assembly since the volume will only decrease when Li_2S is charged.[18,19] However, bulk Li_2S particles still suffer from a large initial activation energy barrier (huge over-potential),[16,20–22] low utilization, and rapid capacity degradation due to its electronic and ionic insulating characteristics and polysulfide dissolution in conjunction with the "shuttle effect."[22–24]

Many strategies have been proposed to circumvent the above issues, such as employing high energy ball-milled or pulsed laser deposition techniques to fabricate Li_2S-metal composites (Li_2S-Fe,[25] Li_2S-Cu,[26] and Li_2S-Co[27] composites) in order to improve the electrical conductivity of Li_2S. However, these methods usually lead to poor electrochemical cyclability as the metal additives convert to metal sulfides during cycling. Li_2S-carbon composites are another widely adopted strategy utilized to overcome the current challenges with employing Li_2S as a cathode. For example, carbon-coated Li_2S core–shell spheres of varying sizes have been synthesized via a two-step chemical vapor deposition (CVD) method[28] and were able to demonstrate a high initial discharge capacity and stable cycling performance over 400 cycles at 0.5C rate without additional carbon additives. Li_2S-C composite with lithium–nitrile interaction has been proposed by uniformly mixing lithium sulfide with polyacrylonitrile (PAN) to form a lithium sulfide-PAN cross-linked matrix,[29] enabling good cycling stability and high Coulombic efficiency.

Dr. G. Zhou, Prof. A. Manthiram
Materials Science and Engineering Program
& Texas Materials Institute
The University of Texas at Austin
Austin, TX 78712, USA
E-mail: rmanth@mail.utexas.edu
Dr. E. Paek, Prof. G. S. Hwang
McKetta Department of Chemical Engineering
University of Texas at Austin
Austin, TX 78712, USA

DOI: 10.1002/aenm.201501355

Other than the post synthesis strategy, a lithiated carbon paper electrode has been employed to chemically reduce Li_2S_6 polysulfide in situ in the liquid electrolyte forming a Li_2S/carbon paper composite,[30] and an in situ formed Li_2S/microporous carbon composite cathode has been fabricated by spraying stabilized lithium-metal powder onto a sulfur/microporous carbon electrode followed by compressing and cell assembly.[31] Both of these techniques demonstrated enhanced cycling stability. However, most of these approaches involved vigorous multistep processes, such as CVD, prelithiation, and battery assembly/disassembly, which are complex and time consuming. Recently, some progress has been made via a solution-based method to ensure that the nanosized Li_2S is uniformly dispersed within a carbon matrix.[32–34] The even distribution effectively decreases the initial activation voltage, shortens the ion diffusion distance, improves the reaction kinetics, and increases cycling performance. Aside from carbon coating, the encapsulation of Li_2S particles using 2D layered materials with high conductivity and strong binding affinity to Li_2S/Li_2S_x species has recently been realized and well-explained by theoretical calculations.[35] However, these advanced electrode materials rely on traditional slurry-casting electrode preparation method that mixes Li_2S based active materials with inactive binders and conductive carbon additives, and then involve casting the mixture onto an aluminum foil current collector. These excess inactive materials and metal current collector naturally decrease the entire energy density of the Li-S cell.

Therefore, a more facile and scalable strategy is urgently needed to design a Li_2S based nanostructured composite with a low energy barrier, good electronic/ionic conductivity, suppressed polysulfide dissolution, and excellent electrochemical performance. Here, we present the development of various Li_2S-coated 3D doped graphene aerogels as a self-supported cathode through a facile liquid infiltration–evaporation coating method for high performance Li-S batteries. The as prepared Li_2S-coated graphene aerogel can be directly used as the current collector thereby acting as both a metal current collector-free and additive/binder-free electrode. The interwoven graphene network promotes rapid electron and ion transfer. The uniformly coated Li_2S over the 3D graphene structure creates shortened ion/electron transport pathways, effectively reducing the energy barrier. The heteroatom nitrogen or boron doping is beneficial for fast charge transfer, and improves the affinity between the nonpolar graphene framework and polar polysulfide species. The heteroatoms additionally demonstrate strong chemical interaction with Li_2S and lithium polysulfides based on the first-principles calculations. Thus, when employing the Li_2S-coated graphene aerogels as cathodes, the Li_2S/(boron or nitrogen)-doped graphene electrodes exhibits significantly improved capacity, cycle stability, and rate capability along with a lowered voltage barrier relative to undoped graphene cathodes.

2. Results and Discussion

Reduced graphene oxide (rGO), boron-doped (B-doped), and nitrogen-doped (N-doped) graphene hydrogels were prepared, respectively, by adding nothing, boric acid (H_3BO_3), and dicyandiamide ($C_2H_4N_4$) as dopants during a hydrothermal reaction, as shown in **Figure 1**a. The graphene-based hydrogels are formed as a robust composite that can be readily sliced into smaller pieces (Figure 1b). After post-lyophilization, the morphologies of the three samples were retained and directly used as freestanding 3D current collectors (Figure S1, Supporting Information). The thickness of the graphene aerogel-based electrodes is around 120–160 µm (Figure S2, Supporting Information) and the densities of the rGO, B-doped graphene, and N-doped graphene aerogels are, respectively, 0.10, 0.09, and 0.07 g cm^{-3}. The fabrication of the Li_2S-coated 3D graphene cathode was achieved by a liquid infiltration–evaporation coating method, as demonstrated in Figure 1c. Li_2S dissolves readily in anhydrous ethanol and graphene aerogels has high liquid absorption abilities. Therefore, a predetermined amount of Li_2S solution was dropped onto both faces of these graphene aerogels. These samples were then heated in the glove box to 260 °C for 30 min in order to completely evaporate any residual ethanol and distribute a uniform Li_2S coating throughout the graphene aerogels. The absorption ability of the porous, interconnecting graphene paired with the boron and nitrogen doping is believed to synergistically

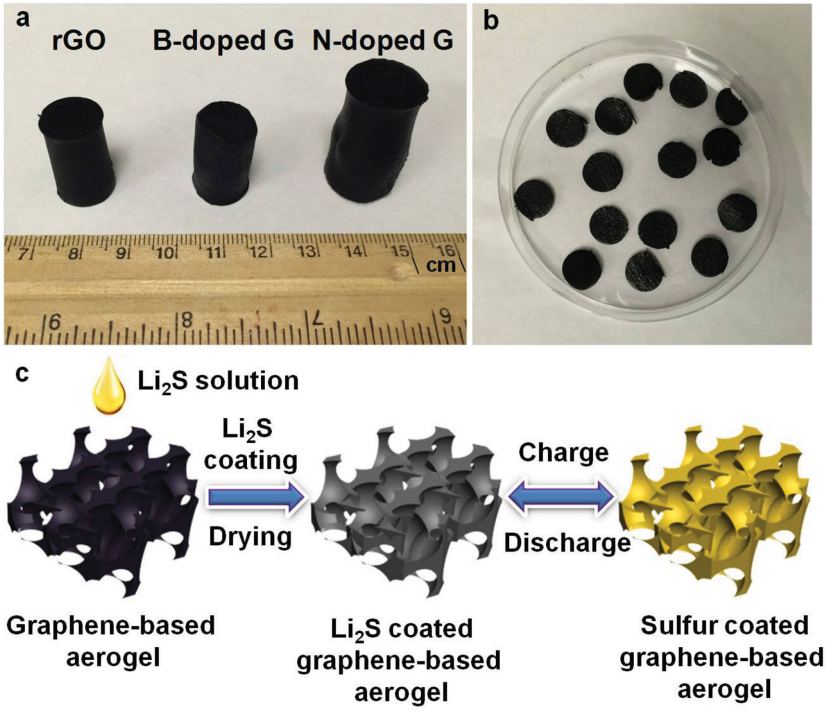

Figure 1. a) Photographs of the rGO, B-doped graphene, and N-doped graphene hydrogels after the hydrothermal reaction (the unit is centimeter for the upper scale). b) Slices of the B-doped graphene hydrogel. c) Illustrations of the Li_2S coating process and the in situ charge/discharge process of the graphene-based electrode.

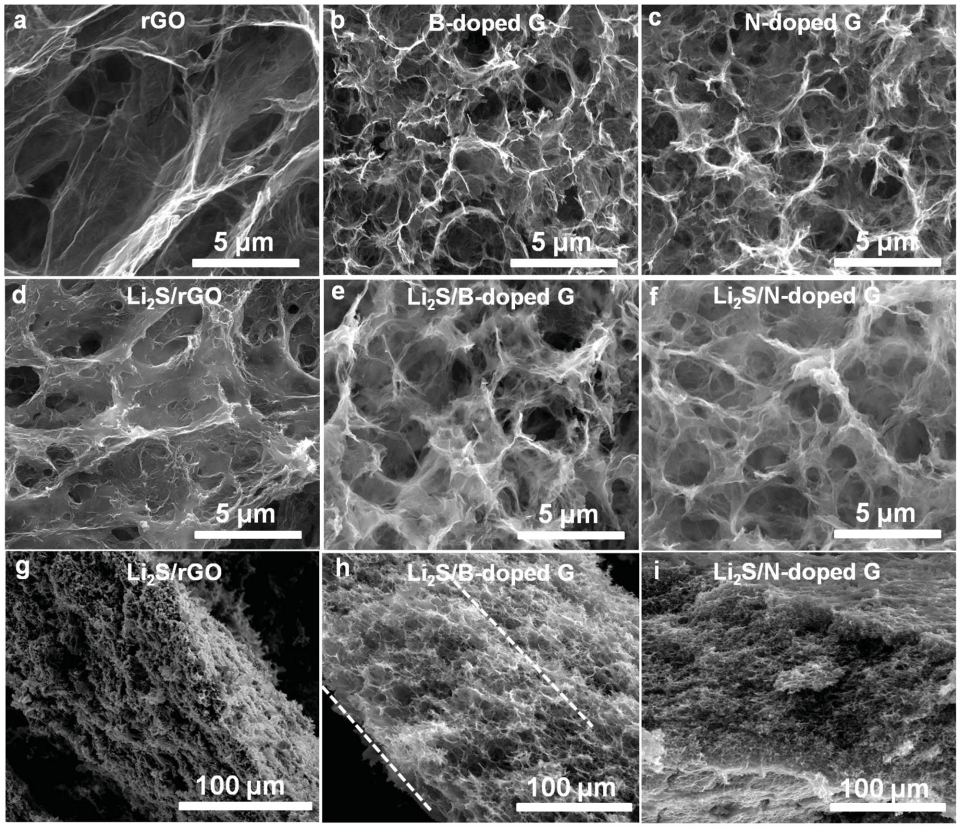

Figure 2. SEM images of the a) rGO, b) B-doped graphene, c) N-doped graphene, d) Li_2S/rGO, e) Li_2S/B-doped graphene, and f) Li_2S/N-doped graphene aerogels. Cross-sectional SEM images of the g) Li_2S/rGO, h) Li_2S/B-doped graphene, and i) Li_2S/N-doped graphene electrodes.

enhance the interactions with lithium polysulfides and Li_2S, thereby effectively improving the electrochemical performance of Li-S batteries (Figure 1c).

Figure 2 details the morphology of both the pristine and the Li_2S-coated graphene aerogels observed with scanning electron microscopy (SEM) techniques. The images show that the as-prepared graphene aerogels exist as an interconnected 3D conductive network with a porous architecture (Figure 2a–c and Figure S3a–c, Supporting Information). The rGO aerogel demonstrates a large pore size in the range of five to tens of micrometers. The thickness of the graphene layers in the aerogel is relatively thick (Figure 2a). In contrast, the pore sizes of the B-doped and N-doped graphene aerogels are smaller with sizes below 10 μm, and a relatively thin graphene layer thickness (Figure 2b,c). High-magnification SEM images illustrate that the B-doped and N-doped graphene aerogels consist of thin and corrugated graphene sheets (**Figure 3**a,b), facile for foreign species deposition and ion accessibility. Scanning transmission electron microscopy (STEM) elemental maps of carbon, boron, and nitrogen clearly reveal that boron or nitrogen heteroatom is homogenously distributed within the graphene sheets (Figure 3c–f). After the Li_2S coating treatment, the 3D framework structure of graphene is well-maintained, while a uniform Li_2S coating layer was observed on the surface of graphene network (Figure 2d–i and Figure S3d–f, Supporting Information), confirmed by the Energy-dispersive X-ray spectroscopy (EDS) element analysis/mapping of carbon and sulfur (Li cannot be detected by EDS, Figures S4 and S5, Supporting Information). This is in contrast to the commercial Li_2S-rGO hybrid in which many exposed Li_2S particles were randomly distributed on the surface of rGO aerogel (Figure S6, Supporting Information). The typical particle size of pristine Li_2S is around tens of micrometers. N_2 isothermal adsorption-desorption analysis (Figure S7, Supporting Information) reveals that the Brunauer–Emmett–Teller (BET) specific surface areas of the rGO, B-doped, and N-doped graphene aerogels are, respectively, 158, 218, and 247 $m^2\ g^{-1}$. The relatively larger BET specific surface areas of the B-doped and N-doped graphene aerogels provide more nucleation sites for the formation of a homogeneous Li_2S coating (Figure 2d–f).

The X-ray diffraction (XRD) patterns of the graphene-based aerogels before and after Li_2S coating are shown in Figure S8 of the Supporting Information and **Figure 4**a. After the hydrothermal reaction, the typical diffraction peak of GO ($2\theta = 11°$) shifts to around 25° for rGO, and B- and N-doped graphene aerogels, indicating the efficient reduction process,[36] as shown in Figure S8 of the Supporting Information. Sharp peaks appear at 27°, 31°, 45°, 53°, 56°, and 66° for commercial Li_2S and commercial Li_2S-rGO hybrid, respectively, corresponding to the (111), (200), (220), (311), (222), and (400) planes of Li_2S (JCPSD No. 01–077–2874), indicating that the pristine commercial Li_2S is highly crystalline. For the coated Li_2S/graphene-based aerogels, the peak of graphene aerogel at ≈26° overlaps with the pristine Li_2S peaks, indicating that the

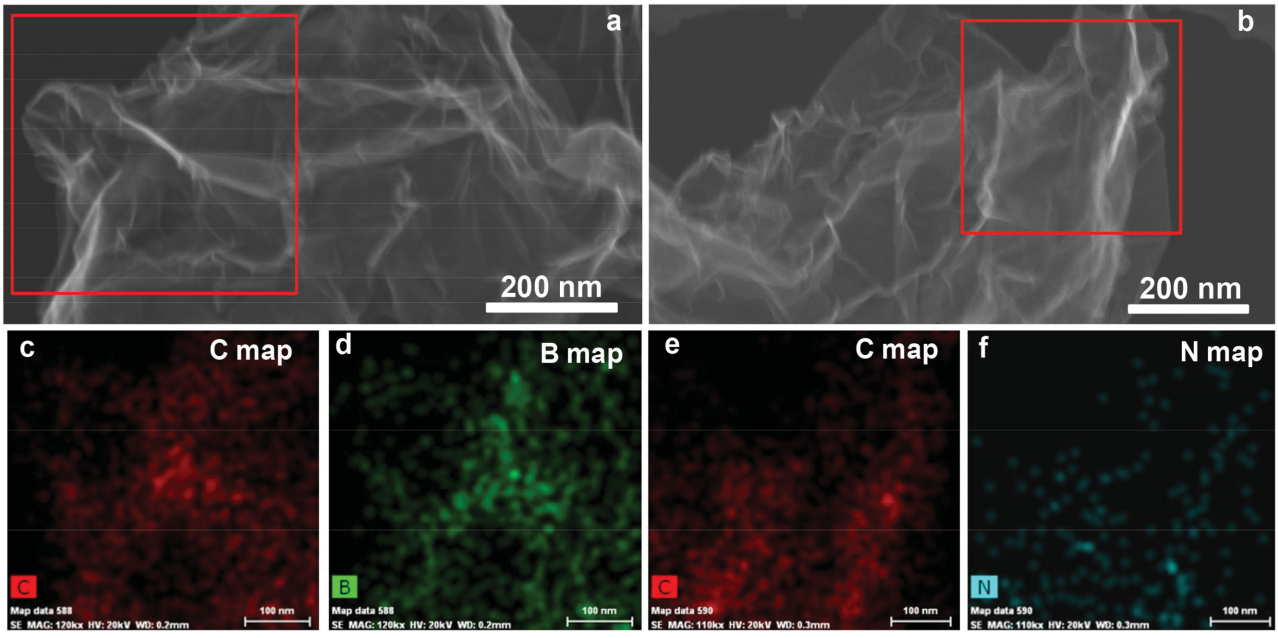

Figure 3. High-magnification SEM image of the a) B-doped graphene and its corresponding c) carbon and d) boron elemental mapping results from the area squared in (a). High-magnification SEM image of the b) N-doped graphene and its corresponding e) carbon and f) nitrogen elemental mapping results from the area squared in (b).

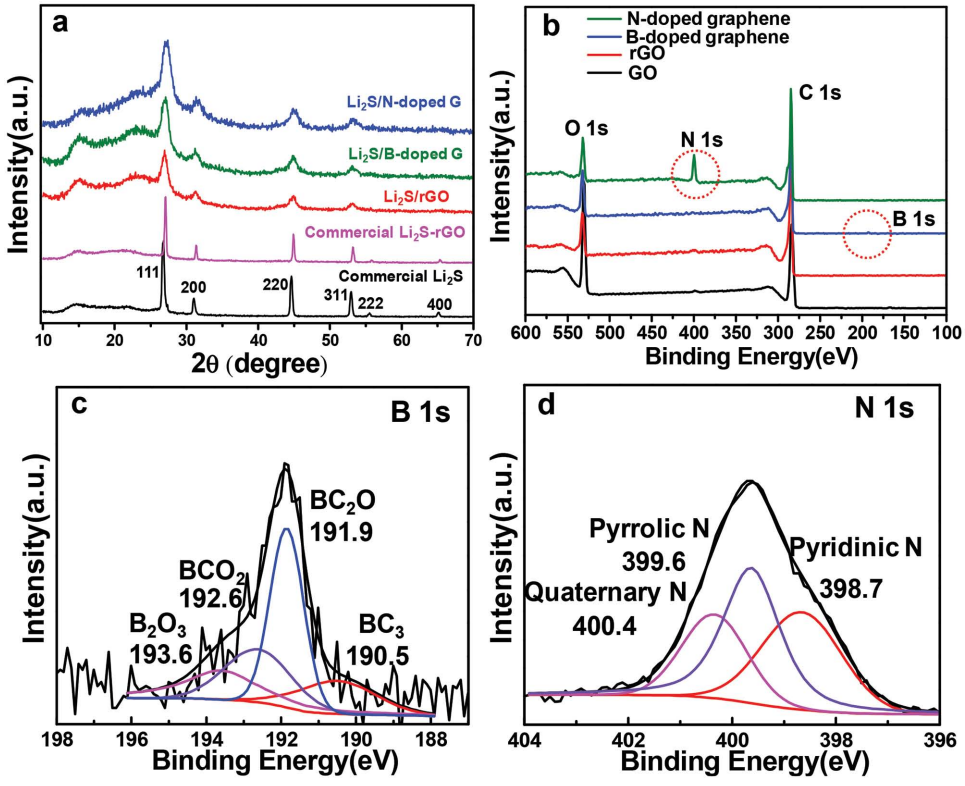

Figure 4. a) XRD patterns of the commercial Li_2S, commercial Li_2S-rGO hybrid, Li_2S/rGO, Li_2S/B-doped graphene, and Li_2S/N-doped graphene aerogels. b) XPS spectra of the surface chemical composition of GO, rGO, B-, and N-doped graphene aerogels. c) XPS spectra of B 1s in B-doped graphene aerogel. d) XPS spectra of N 1s in N-doped graphene aerogel.

Li_2S is successfully incorporated into the graphene network. Peak broadening suggests that the particle sizes of Li_2S are reduced, which is beneficial for decreasing the energy barrier of the Li-S system.[33,34]

X-ray photoelectron spectroscopy (XPS) measurement was used to reveal the surface chemical composition and doped functional groups in the heteroatom-doped graphene aerogels. There is evidence of only C 1s and O 1s signals in the XPS survey of GO and rGO, while the B 1s (binding energy = 192.5 eV) and N 1s (binding energy = 399.8 eV) signals, respectively, emerge in the B-doped and N-doped graphene aerogels,[37,38] implying a successful doping of boron and nitrogen into the carbon backbone (Figure 4b). The doping content is ≈9.8 atom% in the N-doped graphene and ≈1.1 atom% in the B-doped graphene. The C 1s and O 1s XPS profiles of rGO in Figure S9 of the Supporting Information shows the existence of many oxygen-containing functional groups, including C═O (carbonyl), C—OH (hydroxyl), C—O—C (epoxide), and O—C═O (carboxyl) groups.[39] The B 1s spectra of the B-doped graphene can be resolved into four different peaks at the binding energies of 190.5, 191.9, 192.6, and 193.6 eV (Figure 4c), respectively, corresponding to BC_3, BC_2O, BCO_2, and B_2O_3 species.[37,38] Similarly, the high-resolution N 1s spectra of N-doped graphene can be resolved into three different peaks (Figure 4d), which correspond to, respectively, pyridinic N at 398.7 eV, pyrrolic N at 399.6 eV, and quaternary N at 400.4 eV.[40,41] These functional groups are formed predominately through substituting carbon atoms by heteroatoms on edges or defect sites in the basal plane of graphene, which are believed to contribute to the interaction between graphene and lithium polysulfides/Li_2S.

In order to prove the effect of the heteroatom doping and cross-linked porous microstructure, the electrochemical performances of the Li_2S-coated graphene aerogels and commercial Li_2S-rGO hybrid were evaluated in coin cells with a lithium-metal anode and a Celgard 2500 membrane separator. Electrochemical impedance spectroscopy (EIS) was employed to examine the reaction kinetics of these cathodes. The Nyquist plots of all the samples at the open-circuit voltage are composed of a depressed semicircle in the high-medium frequency range and a sloped tail in the low-frequency region (**Figure 5**a), which correspond, respectively, to the charge-transfer resistance (R_{ct}) and Warburg impedance that is related to the ion-diffusion process.[42] The R_{ct} of the Li_2S/N-doped graphene (129.8 Ω) and Li_2S/B-doped graphene (188.9 Ω) electrodes are much lower compared to the commercial Li_2S-rGO hybrid (353.4 Ω) and Li_2S/rGO (254.5 Ω) electrodes, which can be attributed to the favorable charge- and ion-transfer processes from the interconnected graphene framework, heteroatom-doped N or B atoms, and close contact between Li_2S and graphene.

All of the assembled cells were initially charged from open-circuit voltage to 4.0 V at 0.1C rate (1C = 1166 mA g^{-1}, Figure 5b). The commercial Li_2S-rGO hybrid cathode exhibits a high and short initial charging voltage plateau due to the large charge-transfer resistance needed in delithiating the insulating Li_2S particles. By contrast, there was no obvious initial potential barrier for the Li_2S-coated graphene aerogel electrodes during the first charge, with the Li_2S/N-doped graphene electrode, demonstrating the lowest and longest charging voltage plateau. The reduced charge transfer resistance and improved electrochemical activity of Li_2S are consistent with the EIS results. The cyclic voltammetry (CV) profiles were also measured to elucidate the electrochemical behavior of these electrodes (Figure S10, Supporting Information). For Li_2S/N-doped graphene, the initial anodic peak centered around 2.55 V corresponds to the transformation from Li_2S to Li_2S_8 and S,[43] and the value is distinctly lower than that of bulk Li_2S cathode (usually higher than 3.0 V),[16,21] indicating a delithiation process with a significantly lower energy barrier. In the cathodic reduction process for Li_2S/N-doped graphene, the peak at ≈2.35 V can be assigned to the transition between S and soluble lithium polysulfides (Li_2S_x, $4 \le x \le 8$), while the peak at ≈2.01 V is assigned to long-chain polysulfides converting to the insoluble Li_2S_2/Li_2S.[42,44] The potential difference between the cathodic and anodic peaks of the Li_2S/N-doped graphene is smaller than the peaks for commercial Li_2S-rGO hybrid, Li_2S/rGO, and Li_2S/B-doped graphene aerogel, indicating a lower polarization of these electrodes, which is in agreement with the results of galvanostatic charge/discharge profiles (Figure S11, Supporting Information). After the first two cycles, the CV curves overlap without any noticeable peak shift and decrease during the following three scans, indicating the stability and high reversibility of these cathode materials (Figure S12, Supporting Information). The corresponding sulfur elemental mapping characterization (Figure S13, Supporting Information) after CV cycling also confirms the reversible formation of a uniform sulfur coating layer on the surface of the graphene, contributing to the good stability.

After the initial charging at 0.1C rate, the cells were then cycled at 0.3C rate between 1.7 and 2.8 V, as shown in Figure 5c. The Li_2S/doped graphene cathodes exhibit stable cycling performance with high initial specific capacities of 801 mAh g^{-1} for Li_2S/N-doped graphene and 720 mAh g^{-1} for Li_2S/B-doped graphene electrode (based on Li_2S) at 0.3C rate. These initial specific capacities are much higher than that of the Li_2S/rGO, commercial Li_2S-rGO hybrid, and Li_2S-coated conventional Al foil current collector (commercial Li_2S-Al foil, Figure S14a, Supporting Information) electrodes with initial capacities of, respectively, 648, 282, and 414 mAh g^{-1}. After 100 cycles, the capacities are maintained at 635 and 532 mAh g^{-1} for Li_2S-coated N- and B-doped graphene cathodes with nearly 100% Coulombic efficiency. In comparison, the Li_2S/rGO, commercial Li_2S-rGO hybrid, and commercial Li_2S-Al foil electrodes are only able to demonstrate reversible capacities of 395, 89, and 112 mAh g^{-1} after 100 cycles, indicating a higher degree of lithium polysulfide dissolution into the electrolyte. The rate capabilities of these electrodes were evaluated at varying rates from 0.1C to 2C (Figure 5d and Figure S14b, Supporting Information). The Li_2S/doped graphene cathodes demonstrate excellent rate performance with discharge capacities of 561 and 487 mAh g^{-1} for Li_2S/N-doped graphene cathode, and 528 and 395 mAh g^{-1} for Li_2S/B-doped graphene cathode, respectively, at 1C and 2C rates. The rate capacities are significantly better than that of commercial Li_2S-rGO hybrid cathode with only 67 and 22 mAh g^{-1} tested under the same conditions. Moreover, when the C-rate was changed back to 0.5C from 2C rates, the capacity almost recovered to the original capacity for the Li_2S/doped graphene cathodes, an indication of excellent structural stability within the cathode

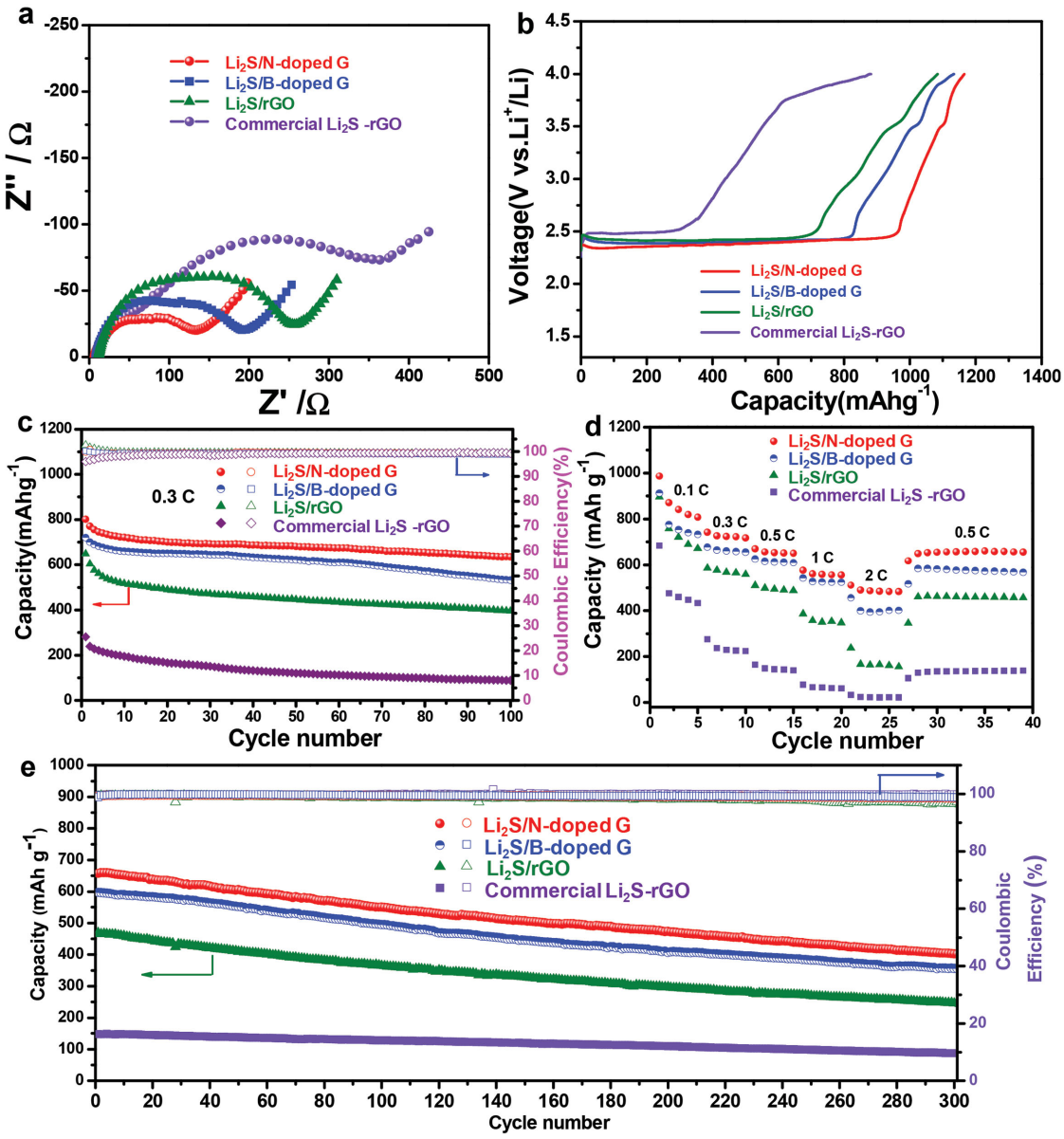

Figure 5. a) Nyquist plots of the commercial Li_2S-rGO hybrid, Li_2S/rGO, Li_2S/B-doped graphene, and Li_2S/N-doped graphene electrodes before cycling from 1 MHz to 100 mHz at room temperature. b) First charge curves of the commercial Li_2S-rGO hybrid, Li_2S/rGO, Li_2S/B-doped graphene, and Li_2S/N-doped graphene electrodes from open-circuit voltage to 4 V. c) Cycling performance and Coulombic efficiency of the commercial Li_2S-rGO hybrid, Li_2S/rGO, Li_2S/B-doped graphene, and Li_2S/N-doped graphene electrodes at 0.3C rate for 100 cycles. d) Rate capability of the commercial Li_2S-rGO hybrid, Li_2S/rGO, Li_2S/B-doped graphene, and Li_2S/N-doped graphene electrodes. e) Long-term cycle stability and Coulombic efficiency of the commercial Li_2S-rGO hybrid, Li_2S/rGO, Li_2S/B-doped graphene, and Li_2S/N-doped graphene electrodes at 0.5C rate for 300 cycles.

matrix. The prolonged cycling performance was evaluated after the rate capability test for 300 charge/discharge cycles, as shown in Figure 5e and Figure S14c of the Supporting Information. The Li_2S/N-doped and Li_2S/B-doped graphene electrodes exhibit stable cycling performance with discharge capacities (initial capacity retention in parenthesis) of 657 (61.3%) and 597 (59.8%) mAh g^{-1} in the first cycle rate and retain capacities of 403 and 357 mAh g^{-1} after 300 cycles at 0.5C rate with an average capacity decay of 0.129% and 0.134% per cycle. By sharp contrast, the Li_2S/rGO, commercial Li_2S-rGO hybrid, and commercial Li_2S-Al foil electrodes exhibit faster capacity fading and poor cycling performance with capacities of only 245, 87, and 65 mAh g^{-1} after 300 cycles, and the related capacity decay are 0.159%, 0.137%, and 0.239% per cycle, demonstrating poor cycling performance. The highly improved cycling and rate performances of the Li_2S/doped graphene cathodes can be attributed to (i) the good dispersion and contact of Li_2S with the interconnected graphene network, (ii) facilitated electron transport pathways from graphene to the insulated Li_2S/S, and (iii) strong binding affinity between doped functional groups and Li_2S/lithium polysulfides to suppress polysulfide dissolution.

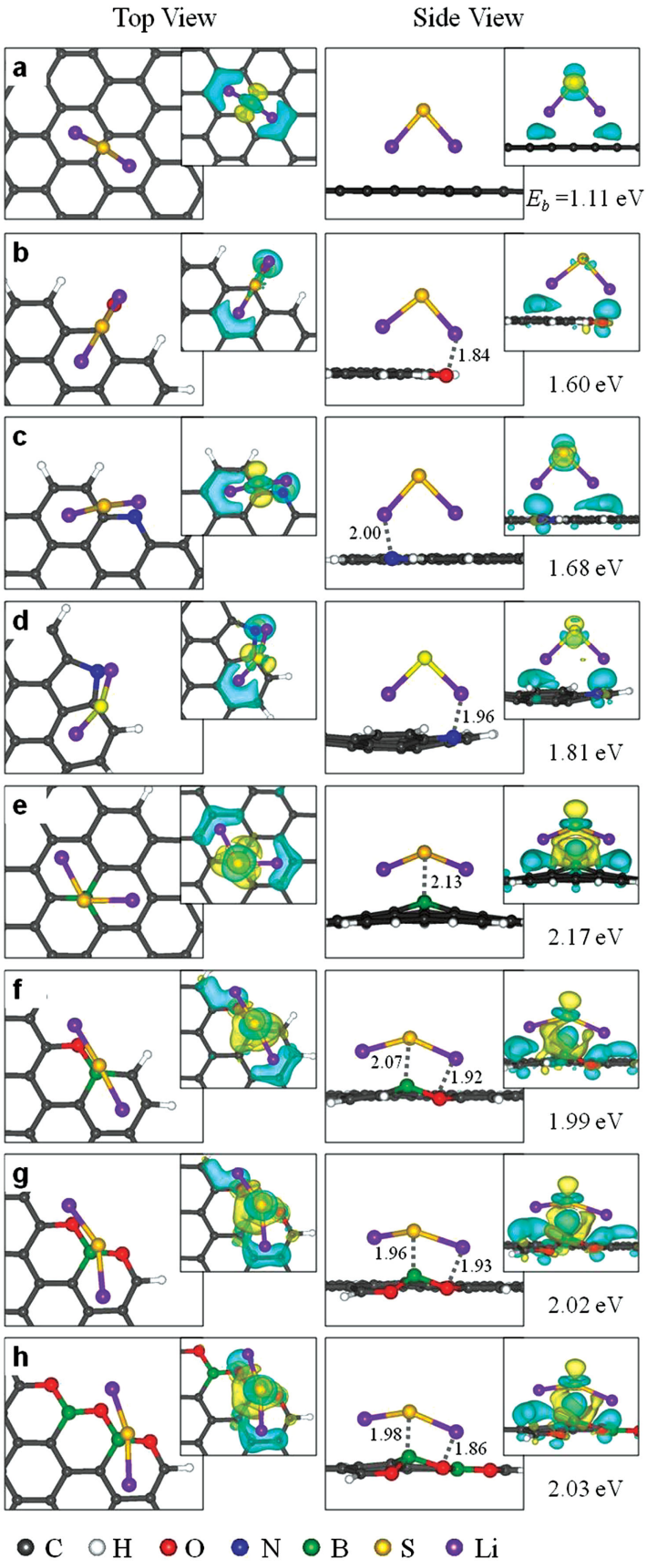

To understand the role of doped atoms on the performance of Li-S batteries, density functional theory (DFT) calculations were performed to examine the interaction between Li_2S and functional groups/heteroatoms in graphene. **Figure 6** shows the optimal adsorption configurations and binding energies of Li_2S at several sites of interest from our DFT-generalized gradient approximation (GGA) calculations. We also considered the monodentate adsorption of Li_2S, as presented in Figure S15 of the Supporting Information; as expected, however, the monodentate states turn out to be far less energetically favorable than the bidentate states in Figure 6. Here, the binding energy is given by $E_b = E_{Li2S} + E_{Gr} - E_{Li2S/Gr}$, where E_{Li2S}, E_{Gr}, and $E_{Li2S/Gr}$ refer, respectively, to the total energies of an isolated Li_2S, the Li_2S-free graphene, and the Li_2S adsorbed graphene. For comparison, we first considered Li_2S adsorption on the basal plane of graphene. As shown in Figure 6a, each Li atom is located on the hollow site above the center of a hexagon. Our Bader charge analysis shows that there is about 0.4e charge transfer from Li_2S to graphene; the transferred charge tends to remain in the regions between the Li and neighboring C atoms, demonstrated by the cyan isosurfaces corresponding to charge gain. The predicted E_b for Li_2S adsorbed on the pristine graphene surface is 1.11 eV.

Our calculations also clearly demonstrate that O and N atoms incorporated at graphene edges (or vacancies) can offer strong binding sites for Li_2S. For instance, as shown in Figure 6, the E_b for Li_2S at the O (in ketone) [(b)], pyridinic N [(c)], and pyrrolic N [(d)] sites are predicted to be, respectively, 1.60, 1.68, and 1.81 eV. Li_2S is adsorbed preferably in the bidentate configuration in which two positively charged Li atoms are respectively placed on top of the negatively charged O (or N) atom and its adjacent hollow site of graphene. The enhancement in the binding strength of lithium sulfides in the presence of O-containing functional groups and N dopants has been also well demonstrated by previous theoretical studies.[39,45–49]

To examine the effect of B doping, we considered several B dopant sites which tend to be available for Li_2S adsorption according to our XPS results (Figure 4), which include substitutional B (BC_3) [(e)] in the basal plane and BC_2O [(f)], BCO_2 [(g)], and B_2O_3 [(h)]

Figure 6. Predicted optimal adsorption configurations of Li_2S at several sites of interest in graphene. a) Basal plane in pristine graphene, b) O in ketone, c) pyridinic N, d) pyrrolic N, e) BC_3, f) BC_2O, g) BCO_2, and h) B_2O_3. Gray, white, red, blue, green, yellow, and purple balls represent, respectively, C, H, O, N, B, S, and Li atoms. For each case, the binding energy (E_b) of Li_2S and selected bond distances (in Å) are also indicated. Charge density difference ($\Delta\rho$) isosurfaces are shown; the cyan and yellow colors indicate the regions of charge gain and loss (of ±0.004 e bohr^{-3}), respectively. Here, $\Delta\rho(r) = \rho_{Li2S/Gr}(r) - [\rho_{Li2S}(r) + \rho_{Gr}(r)]$, where $\rho_{Li2S/Gr}(r)$, $\rho_{Li2S}(r)$, and $\rho_{Gr}(r)$ represent the spatial distributions of charge density, respectively, in the Li_2S adsorbed graphene, an isolated Li_2S, and the Li_2S-free graphene.

complexes at the edge of graphene, as illustrated in Figure 6. Interestingly, the predicted E_b of 1.99–2.17 eV are substantially greater than those at the O and N sites. We find that this is largely attributed to the contribution of additional covalent-like bonding between S and B, as evidenced by the cyan isosurface that represents charge accumulation; it is also worthwhile to note that the B atom is substantially protruded toward the S atom due to the S–B bonding interaction. In this study, the doping amount of boron is 1.1 atom%, much lower compared to nitrogen doping with a value of 9.8 atom%. Higher nitrogen doping content with higher electrical conductivity and more heteroatom active sites contribute to a better electrochemical performance. Nevertheless, the strong binding of Li_2S with B doping species could explain the substantially enhanced cyclic stability in B-doped samples when the B-doping level is only 1.1 atom%. This result is consistent with the previous results that only a small amount of B (0.93 atom%) significantly improves the performance of sulfur/carbon cathode in Li-S batteries.[38]

3. Conclusion

In summary, we have demonstrated a facile synthesis of a high-performance, freestanding Li_2S-coated N- or B-doped graphene aerogel cathode through a liquid infiltration-evaporation coating menthod. As metal current collector/binder-free cathodes, significantly improved capacity, rate performance, and cycle stability have been achieved compared to the undoped ones in Li-S batteries. The enhanced cyclability can be attributed to the (i) strong interactions between the doped graphene and Li_2S/Li_2S_x intermediate species, thereby reducing polysulfide dissolution, (ii) unique cross-linking of the porous structure, facilitating fast electron and ion transport, and (iii) complete Li_2S coating on flexible graphene, accommodating any stress or volume change during cycling and reducing the initial potential barrier of Li_2S. This work provides insight into the application of 3D-functionalized graphene aerogel materials with a strongly bound Li_2S coating in the development of high energy density and long-life rechargeable Li-S batteries.

4. Experimental Section

Synthesis of GO and Graphene-Based Aerogels: GO was synthesized using natural graphite flakes by a modified Hummers' method.[50] For the preparation of rGO aerogel, 60 mL of GO suspension was transferred into a 100 mL Teflon-lined stainless steel autoclave, hydrothermally treated at 180 °C for 12 h, and then cooled to room temperature. The black rGO hydrogel formed was washed with distilled water and freeze-dried to obtain the rGO aerogel. Boron or nitrogen-doped graphene aerogels were prepared with a similar procedure as above but with the addition of 2.5 mmol boric acid (H_3BO_3) or dicyandiamide ($C_2H_4N_4$) as the respective boron and nitrogen dopant into the GO solution, followed by sonication prior to the hydrothermal treatment.

Synthesis of Li_2S-Coated Graphene-Based Aerogels: Commercial Li_2S powder (99.5%, Acros Organics) was purchased and used as received. Li_2S powder was dissolved in anhydrous ethanol, capped, and stirred overnight at room temperature inside an argon-sealed glove box to obtain a 0.55 M Li_2S solution. The graphene-based aerogels were cut, compressed, and shaped into pieces to be used as the current collectors to accommodate Li_2S. The electrical conductivities of the rGO, B-doped graphene, and N-doped graphene are, respectively, 263, 635, and 760 S m^{-1} as tested by the four-probe technique. Because Li_2S is moisture-sensitive, the graphene-based aerogels were first dried at 120 °C under vacuum overnight before being transferred to the glove box (O_2 and H_2O concentration <0.1 ppm) where the Li_2S solution was carefully added. To add the Li_2S solution, the rGO, B-, and N-doped graphene aerogels were placed within a stainless steel cell cap and heated to 260 °C over a heating plate. Li_2S solution (25 µL) was carefully added onto the face of the graphene aerogels until the ethanol had visibly evaporated. The process was repeated, switching between each face with 50 µL units of 0.55 M Li_2S solution in total. These samples were heated at 260 °C for 30 min to completely evaporate off the ethanol and precipitate an even Li_2S coating into the graphene-based aerogel framework.

Materials Characterization: Morphology observations were carried out with a FEI Quanta 650 SEM operated at 20 kV. STEM was performed with a Hitachi S-5500 SEM and EDS collected elemental mapping. Crystal structural characterization was performed with a Philips X-ray diffractometer with Cu Kα radiation (λ = 0.154056 nm) between 10° and 70° at a scan rate of 0.04° s^{-1}. Kapton film was used to protect the air-sensitive Li_2S-coated graphene-based aerogels during the characterization. The electrical conductivity of the graphene-based electrodes was measured by a standard four-point probe resistivity measurement system (S-302–4, Lucas Labs Resistivity, USA). Three measurements were taken at different positions on the sample, and the average value was taken. XPS analysis was performed on a Kratos Analytical spectrometer at room temperature with monochromatic Al Kα (1486.6 eV) radiation. All the spectra were fitted in CasaXPS software after subtraction of a Shirley-type background.

Electrochemical Measurements: CR2032 coin cells were assembled in an argon-filled glove box. The Li_2S-coated graphene-based aerogels were used as self-supported cathode materials with a Li_2S loading of ≈2 mg cm^{-2}, corresponding to a Li_2S content of 50–55 wt% in the whole electrode. For the fabrication of the commercial Li_2S-Al foil electrode, a Li_2S slurry (60 wt% Li_2S as active material, 30 wt% carbon black as conductive agent, and 10 wt% PVDF as binder) was coated onto an Al foil. The Li_2S electrode was cut and shaped into a circular disk with a diameter of 12 mm and was used as a cathode. The mass loading of the Li_2S cathode was 1.8–2.3 mg cm^{-2}. The electrolyte was prepared by dissolving an appropriate amount of lithium trifluoromethanesulfonate ($LiCF_3SO_3$, 98%, Acros Organics, 1 M) and lithium nitrate ($LiNO_3$, 99+%, Acros Organics, 0.1 M) in 1,2-dimethoxyethane (DME, 99+%, Acros Organics) and 1,3-dioxolane (DOL, 99.5%, Acros Organics) (1:1 by volume). 30 µL of the electrolyte was added to wet the Li_2S-coated graphene aerogel cathode. The Celgard 2500 separator was then placed over the electrode and an additional 30 µL of the electrolyte was added to the cell. The lithium-metal foil anode was placed on top of the separator. Galvanostatic cycling measurements were evaluated with an Arbin battery cycler. The cells were initially charged from open-circuit voltage to 4.0 V (vs Li/Li^+) and then cycled between 1.7 and 2.8 V at room temperature. The current densities and calculated specific capacities were based on the mass of Li_2S in the cathode and were varied between 0.1 and 2C rates. Cyclic voltammetry data were collected with an Arbin battery cycler from open-circuit voltage to 4.0 V in the initial cycle and then from 1.7 to 2.8 V in the following cycles with a scan rate of 0.05 mV s^{-1}. Electrochemical impedance spectroscopy (EIS) measurements were performed with a Solartron Impedance Analyzer (Solartron 1260 A) in the frequency range of 1 MHz to 0.1 Hz with an AC voltage amplitude of 5 mV at the open-circuit potential.

Computational Methods: The atomic configurations and binding energies reported herein were calculated using DFT within the Perdew–Berke–Ernzerhof generalized gradient approximation (GGA-PBE),[51] as implemented in the Vienna ab initio simulation package (VASP).[52] We employed the projector augmented wave method to describe the interaction between ion core and valence electrons and a plane-wave basis set with a kinetic energy cutoff of 400 eV. A graphene sheet was modeled using a hexagonal 7 × 7 supercell; we used the GGA-optimized

lattice constant of 2.466 Å, which is close to the experimental value of 2.46 Å. Periodic boundary conditions were employed in all three directions with a vacuum gap of 15 Å in the vertical (z) direction to avoid interactions between graphene and its periodic images. A graphene was described using a flake-like structure consisting of 37 C atoms in a periodic simulation box of dimensions $20 \times 20 \times 15$ Å; all dangling bonds were passivated by H atoms. A gamma-centered $(2 \times 2 \times 1)$ Monkhorst–Pack mesh of *k* points was used for Brillouin zone sampling. Long-range dispersion corrections were taken into account using the semiempirical DFT-D2 approach proposed by Grimme,[53] as implemented in VASP.

Supporting Information

Supporting Information is available from the Wiley Online Library or from the author.

Acknowledgements

This work was funded in part by the Advanced Research Projects Agency-Energy (ARPA-E), U.S. Department of Energy, under Award No. DE-AR0000377. G.S.H. gratefully acknowledges the Robert A. Welch foundation (F-1535) for partial financial support of the computational work and the Texas Advanced Computing Center (TACC) for providing HPC resources. The authors thank Dr. C. Zu for XPS measurements and Dr. Y. Zhao and Ms. P. Han for helpful discussions.

Received: July 7, 2015
Revised: September 20, 2015
Published online: November 16, 2015

[1] P. G. Bruce, S. A. Freunberger, L. J. Hardwick, J.-M. Tarascon, *Nat. Mater.* **2012**, *11*, 19.
[2] A. Manthiram, Y. Fu, S.-H. Chung, C. Zu, Y.-S. Su, *Chem. Rev.* **2014**, *114*, 11751.
[3] Y. Yang, G. Zheng, Y. Cui, *Chem. Soc. Rev.* **2013**, *42*, 3018.
[4] S. Evers, L. F. Nazar, *Acc. Chem. Res.* **2013**, *46*, 1135.
[5] D.-W. Wang, Q. Zeng, G. M. Zhou, L. Yin, F. Li, H.-M. Cheng, I. R. Gentle, G. Q. M. Lu, *J. Mater. Chem. A* **2013**, *1*, 9382.
[6] X. L. Ji, K. T. Lee, L. F. Nazar, *Nat. Mater.* **2009**, *8*, 500.
[7] H.-J. Peng, J.-Q. Huang, M.-Q. Zhao, Q. Zhang, X.-B. Cheng, X.-Y. Liu, W.-Z. Qian, F. Wei, *Adv. Funct. Mater.* **2014**, *24*, 2772.
[8] W. Lv, Z. Li, G. Zhou, J.-J. Shao, D. Kong, X. Zheng, B. Li, F. Li, F. Kang, Q.-H. Yang, *Adv. Funct. Mater.* **2014**, *24*, 3456.
[9] Y. X. Yin, S. Xin, Y. G. Guo, L. J. Wan, *Angew. Chem. Int. Ed.* **2013**, *52*, 13186.
[10] G. M. Zhou, L. Li, D.-W. Wang, X.-y. Shan, S. Pei, F. Li, H.-M. Cheng, *Adv. Mater.* **2015**, *27*, 641.
[11] Z. Li, Y. Huang, L. Yuan, Z. Hao, Y. Huang, *Carbon* **2015**, *92*, 41.
[12] G. Zhou, Y. Zhao, A. Manthiram, *Adv. Energy Mater.* **2015**, *5*, 1402263.
[13] L. Qie, A. Manthiram, *Adv. Mater.* **2015**, *27*, 1694.
[14] X.-B. Cheng, H.-J. Peng, J.-Q. Huang, F. Wei, Q. Zhang, *Small* **2014**, *10*, 4257.
[15] G. Zheng, S. W. Lee, Z. Liang, H.-W. Lee, K. Yan, H. Yao, H. Wang, W. Li, S. Chu, Y. Cui, *Nat. Nanotechnol.* **2014**, *9*, 618.
[16] Y. Yang, G. Y. Zheng, S. Misra, J. Nelson, M. F. Toney, Y. Gui, *J. Am. Chem. Soc.* **2012**, *134*, 15387.
[17] J. Hassoun, B. Scrosati, *Angew. Chem. Int. Ed.* **2010**, *49*, 2371.
[18] Y. Yang, M. T. McDowell, A. Jackson, J. J. Cha, S. S. Hong, Y. Cui, *Nano Lett.* **2010**, *10*, 1486.
[19] Y. Son, J.-S. Lee, Y. Son, J.-H. Jang, J. Cho, *Adv. Energy Mater.* **2015**, *1*, 1500110.
[20] S. Meini, R. Elazari, A. Rosenman, A. Garsuch, D. Aurbach, *J. Phys. Chem. Lett.* **2014**, *5*, 915.
[21] C. Zu, M. Klein, A. Manthiram, *J. Phys. Chem. Lett.* **2014**, *5*, 3986.
[22] C. Wang, X. Wang, Y. Yang, A. Kushima, J. Chen, Y. Huang, J. Li, *Nano Lett.* **2015**, *15*, 1796.
[23] L. Wang, Y. Wang, Y. Xia, *Energy Environ. Sci.* **2015**, *8*, 1551.
[24] K. Cai, M.-K. Song, E. J. Cairns, Y. Zhang, *Nano Lett.* **2012**, *12*, 6474.
[25] M. N. Obrovac, J. R. Dahn, *Electrochem. Solid State Lett.* **2002**, *5*, A70.
[26] A. Hayashi, R. Ohtsubo, T. Ohtomo, F. Mizuno, M. Tatsumisago, *J. Power Sources* **2008**, *183*, 422.
[27] Y. Zhou, C. Wu, H. Zhang, X. Wu, Z. Fu, *Electrochim. Acta* **2007**, *52*, 3130.
[28] C. Nan, Z. Lin, H. Liao, M.-K. Song, Y. Li, E. J. Cairns, *J. Am. Chem. Soc.* **2014**, *136*, 4659.
[29] J. Guo, Z. Yang, Y. Yu, H. D. Abruña, L. A. Archer, *J. Am. Chem. Soc.* **2013**, *135*, 763.
[30] Y. Fu, C. Zu, A. Manthiram, *J. Am. Chem. Soc.* **2013**, *135*, 18044.
[31] S. Zheng, Y. Chen, Y. Xu, F. Yi, Y. Zhu, Y. Liu, J. Yang, C. Wang, *ACS Nano* **2013**, *7*, 10995.
[32] F. Wu, J. T. Lee, A. Magasinski, H. Kim, G. Yushin, *Part. Part. Syst. Char.* **2014**, *31*, 639.
[33] F. Wu, H. Kim, A. Magasinski, J. T. Lee, H.-T. Lin, G. Yushin, *Adv. Energy Mater.* **2014**, *4*, 1400196.
[34] K. Zhang, L. Wang, Z. Hu, F. Cheng, J. Chen, *Sci. Rep.* **2014**, *4*, 6467.
[35] Z. W. Seh, J. H. Yu, W. Li, P.-C. Hsu, H. Wang, Y. Sun, H. Yao, Q. Zhang, Y. Cui, *Nat. Commun.* **2014**, *5*, 5017.
[36] S. Pei, H.-M. Cheng, *Carbon* **2012**, *50*, 3210.
[37] Z.-S. Wu, A. Winter, L. Chen, Y. Sun, A. Turchanin, X. Feng, K. Müllen, *Adv. Mater.* **2012**, *24*, 5130.
[38] C.-P. Yang, Y.-X. Yin, H. Ye, K.-C. Jiang, J. Zhang, Y.-G. Guo, *ACS Appl. Mater. Interfaces* **2014**, *6*, 8789.
[39] G. M. Zhou, L.-C. Yin, D.-W. Wang, L. Li, S. Pei, I. R. Gentle, F. Li, H.-M. Cheng, *ACS Nano* **2013**, *7*, 5367.
[40] Y. Zheng, Y. Jiao, L. Ge, M. Jaroniec, S. Z. Qiao, *Angew. Chem. Int. Ed.* **2013**, *52*, 3110.
[41] G. Zhou, E. Paek, G. S. Hwang, A. Manthiram, *Nat. Commun.* **2015**, *6*, 7760.
[42] G. M. Zhou, S. Pei, L. Li, D.-W. Wang, S. Wang, K. Huang, L.-C. Yin, F. Li, H.-M. Cheng, *Adv. Mater.* **2014**, *26*, 625.
[43] Z. Yuan, H.-J. Peng, J.-Q. Huang, X.-Y. Liu, D.-W. Wang, X.-B. Cheng, Q. Zhang, *Adv. Funct. Mater.* **2014**, *24*, 6105.
[44] R. Elazari, G. Salitra, A. Garsuch, A. Panchenko, D. Aurbach, *Adv. Mater.* **2011**, *23*, 5641.
[45] J. Song, T. Xu, M. L. Gordin, P. Zhu, D. Lv, Y.-B. Jiang, Y. Chen, Y. Duan, D. Wang, *Adv. Funct. Mater.* **2014**, *24*, 1243.
[46] H.-J. Peng, T.-Z. Hou, Q. Zhang, J.-Q. Huang, X.-B. Cheng, M.-Q. Guo, Z. Yuan, L.-Y. He, F. Wei, *Adv. Mater. Interfaces* **2014**, *1*, 1400227.
[47] Z. Wang, Y. Dong, H. Li, Z. Zhao, H. Bin Wu, C. Hao, S. Liu, J. Qiu, X. W. Lou, *Nat. Commun.* **2014**, *5*, 5002.
[48] B. Wang, S. M. Alhassan, S. T. Pantelides, *Phys. Rev. Appl.* **2014**, *2*, 034004.
[49] L. W. Ji, M. M. Rao, H. Zheng, L. Zhang, Y. Li, W. Duan, J. Guo, E. J. Cairns, Y. Zhang, *J. Am. Chem. Soc.* **2011**, *133*, 18522.
[50] J. Zhao, S. Pei, W. Ren, L. Gao, H.-M. Cheng, *ACS Nano* **2010**, *4*, 5245.
[51] J. P. Perdew, K. Burke, M. Ernzerhof, *Phys. Rev. Lett.* **1996**, *77*, 3865.
[52] G. Kresse, J. Furthmüller, *VASP*, Vienna University of Technology, Vienna **2001**.
[53] S. Grimme, *J. Comput. Chem.* **2006**, *27*, 1787.

